INTERNATIONAL JOURNAL FOR NUMERICAL METHODS IN FLUIDS
Int. J. Numer. Meth. Fluids 2006; **52**:499–527
Published online 24 February 2006 in Wiley InterScience (www.interscience.wiley.com). DOI: 10.1002/fld.1178

CFD-based multi-objective optimization method for ship design

Yusuke Tahara*,†, Satoshi Tohyama‡ and Tokihiro Katsui§

Osaka Prefecture University, Japan

SUMMARY

This paper concerns development and demonstration of a computational fluid dynamics (CFD)-based multi-objective optimization method for ship design. Three main components of the method, i.e. computer-aided design (CAD), CFD, and optimizer modules are functionally independent and replaceable. The CAD used in the present study is NAPA system, which is one of the leading CAD systems in ship design. The CFD method is FLOWPACK version 2004d, a Reynolds-averaged Navier–Stokes (RaNS) solver developed by the present authors. The CFD method is implemented into a self-propulsion simulator, where the RaNS solver is coupled with a propeller-performance program. In addition, a maneuvering simulation model is developed and applied to predict ship maneuverability performance. Two nonlinear optimization algorithms are used in the present study, i.e. the successive quadratic programming and the multi-objective genetic algorithm, while the former is mainly used to verify the results from the latter. For demonstration of the present method, a multi-objective optimization problem is formulated where ship propulsion and maneuverability performances are considered. That is, the aim is to simultaneously minimize opposite hydrodynamic performances in design tradeoff. In the following, an overview of the present method is given, and results are presented and discussed for tanker stern optimization problem including detailed verification work on the present numerical schemes. Copyright © 2006 John Wiley & Sons, Ltd.

KEY WORDS: CAD; RaNS solver; hull-form optimization; multi-objective genetic algorithm; maneuverability; propulsion

1. INTRODUCTION

Currently, computational fluid dynamics (CFD) is used as an analysis tool to study alternative ship hull-form designs. Although extremely valuable, this approach suffers the limitation that

*Correspondence to: Y. Tahara, Marine System Engineering, Osaka Prefecture University, Sakai, Japan.
†E-mail: tahara@marine.osakafu-u.ac.jp
‡E-mail: Satoshi_Tohyama@marine.osakafu-u.ac.jp
§E-mail: kastui@marine.osakafu-y.ac.jo

Contract/grant sponsor: U.S. Office of Naval Research; contract/grant numbers: N000140210256, N000140510616

Received 30 August 2005
Revised 12 December 2005
Accepted 14 December 2005

it does not identify the optimum design. This is the background for developing CFD-based optimization methods wherein automatic determination of optimum shape is part of the simulation. Such approaches with complex CFD analysis have been developed by the present authors and colleagues [1–12], where the main emphasis is placed on utilization of advanced geometry modelling and high-fidelity Reynolds-averaged Navier–Stokes (RaNS) equation solver [1–10], including consideration of complexity of a real-life design problem, conditions, and constraints, and comprehensive evaluation of the results through model test verification [11, 12]. Besides works cited above, other recent applications of CFD-based optimization [13–18] witness that optimal shape design is receiving growing consideration in the naval hydrodynamics community, filling the gap with other fields (automotive, aeronautical, etc.) at a fast pace.

One of important components of the CFD-based optimization is a geometry modelling method to provide a link between the design variables and a hull form. More specifically, the parametric expression and modification of the ship hull form is an essential feature for the automatic optimization. However, in most of the related studies, solutions of the optimization schemes are not directly linked with computer-aided design (CAD) model actually used by hull-form designers (see Reference [5] for more complete survey). The limitation leads to a fact that modification trends proposed by the optimization schemes are often far from those designers can accept. More advanced and capable approach must be introduced in the optimization scheme, i.e. implementation of the direct link with designer's CAD system for the CAD-based hull-form modification is necessary.

On the other hand, the optimal design of the hull shape is basically a multi-criteria (or multi-objective) problem. For instance, goals of the design process can be resistance reduction, low noise, minimal wave height, reduced amplitude and acceleration of particular motions, etc. In addition, ship designers may also be interested to enhance certain quantities related to the engine power or to the maintenance costs. Unfortunately, the improvement of a specific aspect of the global design usually causes the worsening for some others, that is to say the optimal design of a ship hull is a multi-objective optimization problem. Therefore, the correct approach to the problem must follow the multi-objective optimization theory and the present work represents an attempt to develop such a procedure for ship design, involving the modelling, the development and the implementation of algorithms for the hydrodynamic optimization.

This paper concerns development and demonstration of a CFD-based multi-objective optimization method for ship design. Main objective of the present study is a system development and demonstration of the capability, which justifies use of simplified conditions, e.g. static sinkage and trim, and simplified design constraints. Three main components of the method, i.e. CAD, CFD, and optimizer modules are functionally independent and replaceable. The CAD used in the present study is NAPA system [19], which is one of leading CAD systems in ship design. In combination with the CAD model, a practical hull-form modification method is proposed, i.e. that is based on one-parameter hull-form blending and two-parameter prismatic curve control, where the latter is an extension of an original scheme used in may shipyards [20]. The CFD method is FLOWPACK version 2004d, a RaNS solver developed by the authors [21–23]. The CFD method is implemented into a self-propulsion simulator [23], where the RaNS solver is coupled with a propeller-performance program based on infinitely bladed propeller theory [24] in an interactive and iterative manner. In addition, a maneuvering simulation model is developed and applied to predict ship maneuverability performance, where the results are verified through comparison with experimental data [25]. Two nonlinear optimization algorithms are used in the present study, i.e. the successive

quadratic programming (SQP) [1–5] and the multi-objective genetic algorithm (MOGA) [12, 26], while the former is mainly used to verify the results from the latter. For demonstration of the present method, a multi-objective optimization problem is formulated where ship propulsion and maneuverability performances are considered. That is, the aim is to simultaneously minimize opposite hydrodynamic performances in design tradeoff, i.e. delivered horsepower (DHP) and the first overshoot angle in (OSA) 10/10-degree-Zigzag test obtained from the self-propulsion simulator and maneuvering simulation method, respectively. In the following, an overview of the present method is given, and results are presented and discussed for tanker stern optimization problem including detailed verification work on the present numerical schemes.

2. OVERVIEW OF COMPUTATIONAL METHOD

To develop CFD-based optimization methods, three main components must be built and are common among many different applications (see Figure 1): first, a method to solve the nonlinear optimization problem formed by the objective and the constraint functions; second, a geometry modelling method to provide a link between the design variables and a body shape; and third, a CFD solver used as analysis tool to return the value of the objective function and of functional constraints. In the present study, a CAD-based hull-form modification method will be adopted. Two approaches are possible, i.e. CAD direct control and CAD emulation approaches. Those are illustrated in Figure 2, i.e. systems 1 and 2, respectively. In the former, optimizer directly executes CAD macro-file in which the procedures of hull-form modification, geometry analysis, and CFD pre-processing are described. In the latter, a module is implemented in order to emulate CAD operation based on the same mathematical surface modelling (e.g. NURBS), and data I/O follows a universal data structure, e.g. IGES format. The two approaches offer advantage in different aspects, i.e. the former is more straightforward in implementation into design work, and the latter more independent from CAD system itself. The authors recently demonstrated both approaches, i.e. in Reference [1] and References [11, 12], respectively.

In the present study, the system 1 is used. Earlier version of the optimization module was demonstrated in Reference [1]. Optimization system parameters, e.g. number of design parameters, optimization algorithm, and definition of objective and constraint functions, can be specified in spreadsheet screen. See Reference [1] for more detailed features including

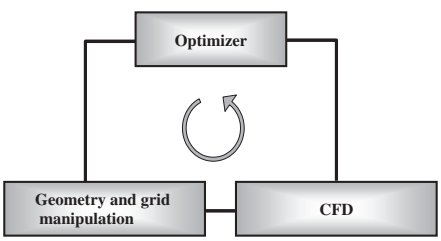

Figure 1. Basic elements of a CFD-based optimization environment.

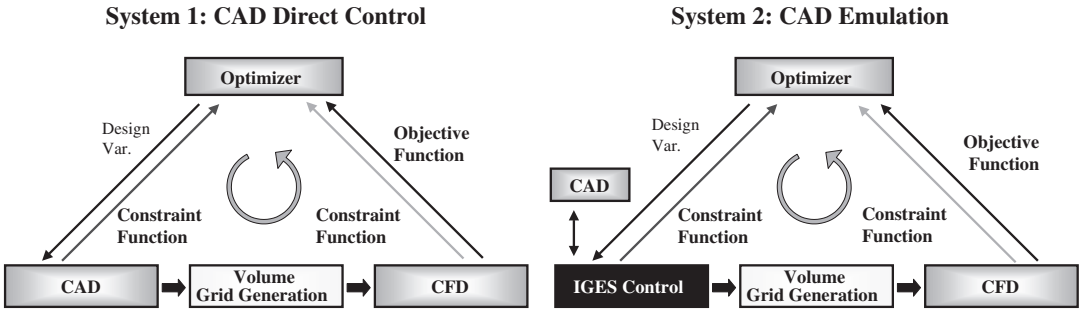

Figure 2. Implementation of CAD-based hull-form modification into optimization environment. System 1—CAD direct control approach and System 2—CAD emulation approach, left and right, respectively.

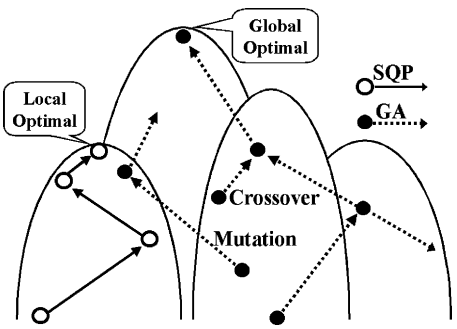

Figure 3. Comparison of strategy in optimal search between SQP and GA approaches.

EXE/DLL file interfaces and the network-passage protocol. In the present study, new features based on MOGA algorithm for solution to multi-objective optimization problem are included. An overview of the present schemes is given in the following.

2.1. Optimization method

Two optimization algorithms are used in the present study, i.e. SQP [1–5] and MOGA [12, 26], whereas the former is mainly used to verify the results from the latter. Figure 3 illustrates differences in strategy between SQP and GA. SQP is able to efficiently search optimal if the initial point is correctly given. In contrast, GA is capable for global optimal search, and does not require evaluation of gradients. Another important feature of GA is that it can be extended to find Pareto-optimal solutions in multi-objective optimization. After the Pareto optimal is determined, a simple decision maker theory can be used to select final solution on the set. In the following, an overview of the present optimization scheme is given.

2.1.1. Single-objective optimizer—SQP approach. The present single-objective optimization method is based on SQP algorithm. A general expression of the single-objective optimization

problem is defined as follows:

$$\text{Min} \quad \lfloor F(\boldsymbol{\beta}; Rn, Fn) \rfloor_{Rn,Fn} \tag{1}$$

$$\text{s.t.} \quad H_i(\boldsymbol{\beta}) \geqslant 0 \quad (i = 1, 2, \ldots, q) \tag{2}$$

where $\boldsymbol{\beta} = (\beta_1, \beta_2, \ldots, \beta_k)$ are design parameters, F is the objective function to be minimized, and H_i are inequality constraint functions. In SQP scheme, the objective and constraint functions are approximated in quadratic form such that

$$\text{Min} \quad [\nabla F(\boldsymbol{\beta}; Rn, Fn)^{\mathrm{T}} \mathbf{d} + \tfrac{1}{2} \mathbf{d}^{\mathrm{T}} B \mathbf{d}]_{Rn,Fn} \tag{3}$$

$$\text{s.t.} \quad H_i(\boldsymbol{\beta}) + \nabla H_i(\boldsymbol{\beta})^{\mathrm{T}} \mathbf{d} = 0 \quad (i = 1, 2, \ldots, q) \tag{4}$$

where $\mathbf{d} = (d_1, d_2, \ldots, d_k)$ is the direction vector, and B is the approximate Hessian matrix of the Lagrangian. In each optimization cycle (n), optimum $\mathbf{d}$ is obtained so as to minimize F, and $\boldsymbol{\beta}$ is updated by $\boldsymbol{\beta}^{n+1} = \boldsymbol{\beta}^n + \mathbf{d}$. In the present study, the derivative terms in the above equations are evaluated by a second-order central finite difference scheme. Advantage of SQP over SLP (successive linear programming) was shown in the author's precursory work, and quite a few demonstrations with SQP were performed for optimization of tanker hull-form and naval surface combatant [1–5]. Reference [27] is recommended for more details of SQP.

2.1.2. Multi-objective optimizer—MOGA approach. Next, solution scheme for multi-objective optimization problem is described. A general expression of N-objective function optimization problem is defined as follows:

$$\text{Min} \quad \begin{cases} [F_1(\boldsymbol{\beta}; Rn, Fn)]_{Rn,Fn} \\ [F_2(\boldsymbol{\beta}; Rn, Fn)]_{Rn,Fn} \\ \qquad \vdots \\ [F_N(\boldsymbol{\beta}; Rn, Fn)]_{Rn,Fn} \end{cases} \tag{5}$$

$$\text{s.t.} \quad H_i(\boldsymbol{\beta}) \geqslant 0 \quad (i = 1, 2, \ldots, q) \tag{6}$$

In the present study, the adopted scheme is an extended genetic algorithm (GA) [28–30] for multi-objective optimization problem, i.e. MOGA. The basic procedure follows that of GA: (i) generation of an initial population of individuals at random manner; (ii) decoding and evaluation of some predefined quality criterion, referred to as the fitness; (iii) selection of individuals based on a probability proportional to their relative fitness; (iv) crossover and mutation. The steps (ii)–(iv) are repeated until the generation achieves designated number.

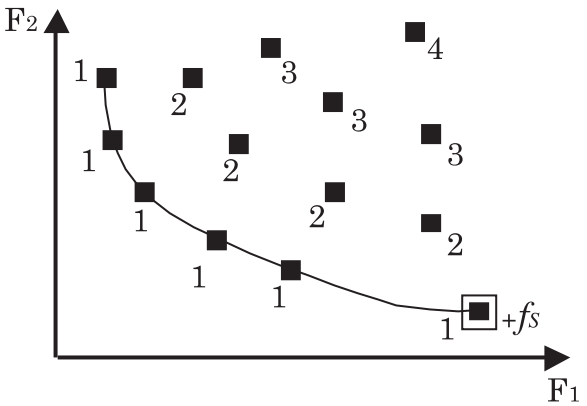

Figure 4. Pareto ranking and sharing operations. Fitness is given based on Pareto ranking, and additive fitness is considered based on uniformity of individual distribution on Pareto-optimal set. These are used in MOGA.

The extension of GA for MOGA is straightforward. Main goal is to detect uniformly distributed globally Pareto-optimal front. Definition of globally Pareto-optimal set is as follows: the nondominated set of the entire feasible search space is the globally Pareto-optimal set [30]. In order to make the conditions of Pareto optimality mathematically rigorous, we state that a vector $\mathbf{x}$ is particularly less than $\mathbf{y}$, symbolically $\mathbf{x} < P\mathbf{y}$ when the following condition holds: $(\mathbf{x} < P\mathbf{y}) \Leftrightarrow (\forall i)(x_i \leqslant y_i) \wedge (\exists i)(x_i < y_i)$. Under this circumstance, we say that point $\mathbf{x}$ dominates point $\mathbf{y}$. If a point is not dominated by any other, we say that it is nondominated or noninferior. The basic definition is used to find noninferior points in MOGA in association with Pareto-ranking technique and sharing method in the present study. At each generation, higher fitness f_{O} is given to individuals of higher Pareto ranking R_{P}, and at the same time, additive fitness f_{S} is given to individual with the best quality in one of objective functions (see Figure 4 for example of two-objective function case), i.e. $f_{\mathrm{O}} = 1/R_{\mathrm{P}} + f_S$. The functional constraints are accounted for by using a penalty function approach, which artificially lowers the fitness if the constraints are violated and is expressed as

$$f = f_{\mathrm{O}} - r\left[\sum_{j=1}^{M} |h_j(x)| + \sum_{j=1}^{N} |\min\{0, -g_j(x)\}|\right] \tag{7}$$

At present, the GA and MOGA schemes can be used in both parallel and serial modes. The authors developed parallel-computing GA and MOGA by introducing message passing interface (MPI) protocol [31] (see Figure 5), and demonstrated single and multi-objective optimizations of naval surface combatant [11, 12]. It was shown that both GA and MOGA schemes yield satisfactory results. Introduction of parallel architecture effectively enhanced computational speed. Figure 6 shows results from the initial evaluation of the scheme, where sufficiently fast convergence towards analytically given Pareto-optimal front is indicated. In addition, the author and colleagues evaluated relative performance of the present MOGA scheme to others [26] by using more complex six algebraic test functions. Figure 7 shows some representative results from the work. The test functions T_1 (Equation (8), $N = 2$) and

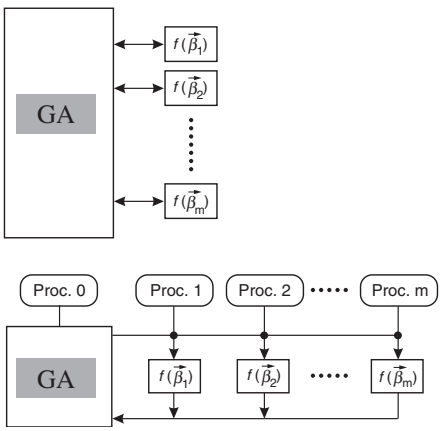

Figure 5. Serial and parallel architectures for GA optimizer. The conventional GA algorithm has been extended for high-performance optimization method by introducing parallel computing.

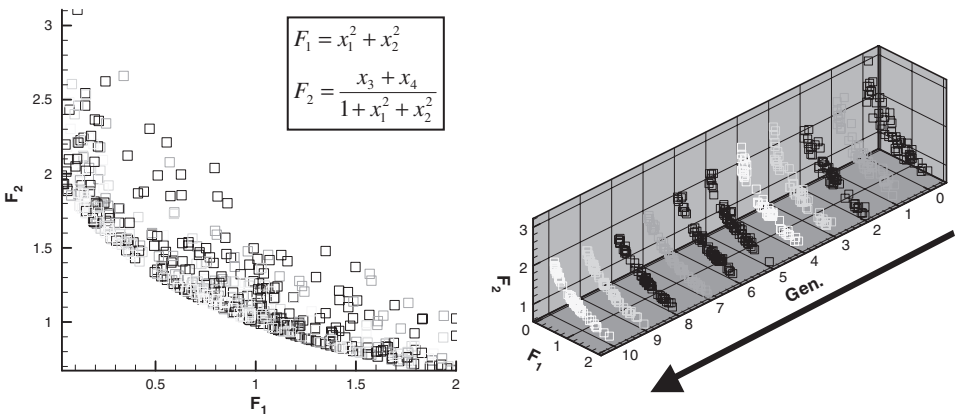

Figure 6. MOGA results. Determination of Pareto front and convergence of the individuals to the front for an algebraic test function. Sufficiently fast convergence is demonstrated for this test case.

T_6 (Equation (9), $N = 30$) have a convex Pareto-optimal front, and a Pareto-optimal front consisting of several noncontiguous convex parts, respectively.

$$\begin{aligned} f_1(\vec{x}) &= x_1 \\ f_2(\vec{x}) &= H(1 - \sqrt{f_1(\vec{x})/H}) \end{aligned} \tag{8}$$

$$\begin{aligned} f_1(\vec{x}) &= x_1 \\ f_2(\vec{x}) &= H(1 - \sqrt{f_1(\vec{x})/H}) - f_1(\vec{x}) \sin(10\pi f_1(\vec{x})) \end{aligned} \tag{9}$$

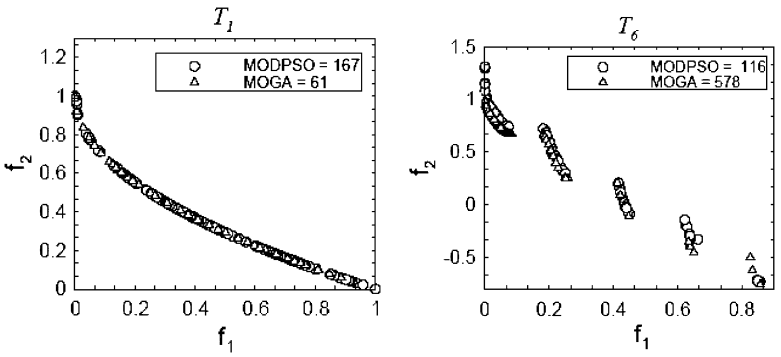

Figure 7. Comparative results on the algebraic test functions. Test functions T_1 ($N = 2$) and T_6 ($N = 30$) have a convex Pareto front and a discrete Pareto front, respectively. Performance of the present MOGA approach is shown equivalent to that of MODPSO scheme.

where

$$H = 1 + \frac{9}{N-1}\sum_{i=2}^{N} x_i \tag{10}$$

Being focused on multi-objective problems with expensive objective functions, we decided to fix the maximum number of function evaluations to $100N$. Bounds on the value of the design variables are also applied ($0 \leqslant x_i \leqslant 1$). As indicated in Figure 7, performance of the present MOGA is shown equivalent to that of one of the advanced deterministic optimization scheme, a multi-objective deterministic particle swarm optimization (MODPSO) scheme [26]. Reader may refer to Reference [30] for more various test problems.

2.2. Geometry modelling method

In ship design, a figure named *body plan* is used to show the shapes of sections determined by the intersection of the hull-form with planes perpendicular to the longitudinal axis. Figure 8 shows the body plan for ships used in the present study. As is the case for those ships, most ships are symmetrical about the centreplane, and the body plane shows only a half part of ship. In this paper, the centreplane intersection is referred to as the profile. Body plan stations are customarily numbered from stern to bow (particularly in European and Japanese shipyards) such that the fore and after maximum stations are S.10 (forward perpendicular—FP) and S.0 (after perpendicular—AP), respectively. Also, section at S.5 is called midship section. In the present study, the FP and AP, respectively, correspond to $x = 0$ and 1 in computational coordinates. Another important hull-form characteristic in ship design is a prismatic curve (often referred to as C_p curve), which shows longitudinal distribution of sectional area of ship. Figure 9 shows an example of the curve. In many modern vessels, particularly cargo or tanker vessels, the form of cross-section below the design waterline extends without change for some distance in forebody an afterbody usually including midship location. Such vessels are said to have parallel middle body, which is also the case for the present ships discussed below. In the following, geometry modelling method used in the present study is described.

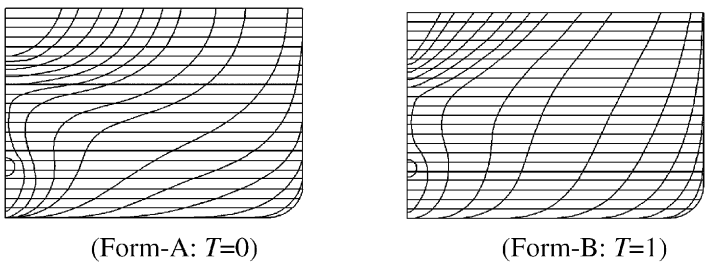

Figure 8. Comparison of body plan for SR221A and SR221B hulls. Left and right are SR221A and SR221B, respectively, while forebody is same between the two hulls. The blending parameters (T) are 0 and 1. Stern frame lines are more V and U types, respectively. Propulsive factors $1+k$ and $1-w_n$ are smaller and larger for A form.

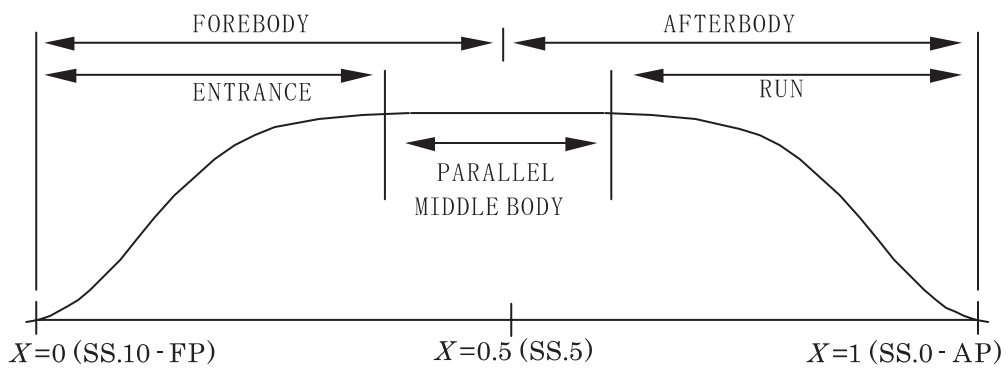

Figure 9. Geometry of sectional area curve for ship. $X=0$ and 1 correspond to FP (forward perpendicular, SS.10), and AP (after perpendicular, SS.0), respectively. $X=0.5$ (SS.5) is called midship section. Sectional area is constant in parallel middle body.

2.2.1. CAD module (NAPA). The CAD module used in the present work is NAPA system [19]. As mentioned earlier, an important feature for the automatic optimization is the parametric expression and modification of the ship hull-form, which is apparently a key feature of NAPA system. Figure 10 shows an example for the parametric definition of SR221A tanker hull form, a basic hull-form used in the present study. The NAPA Macro is used to aid interfaces among CAD, optimizer, and CFD modules. In the NAPA Macro, the procedures of hull-form modification, geometry analysis, and CFD pre-processing are also described. Reference [1] includes a detailed example for the description. In combination with the CAD model, a practical hull-form modification method is proposed, i.e. that is based on one-parameter hull-form blending and two-parameter prismatic-curve control. These approaches are described in the following.

2.2.2. Hull-form blending (morphing) approach. New hull form is defined by blending of two (or more) basic hull-forms through blending parameter. This approach is also referred to as *morphing*. The basic hull-forms are defined by same numbers of control points. In the

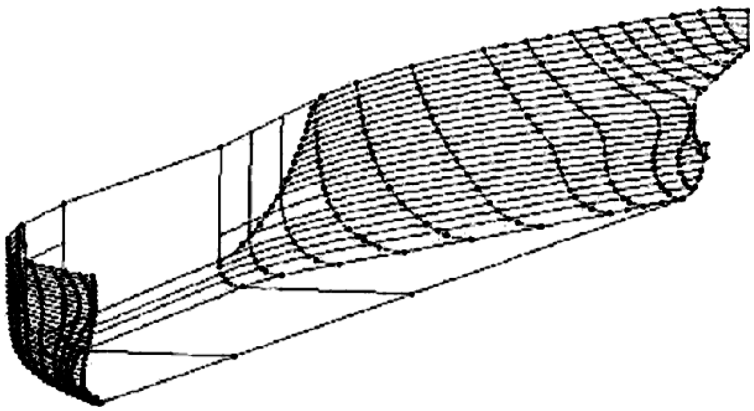

Figure 10. Parametric expression of SR221A tanker hull form by NAPA system.

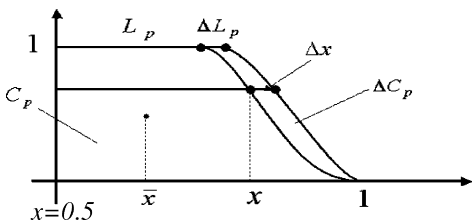

Figure 11. Parametric modification of prismatic curve (C_p curve).

present work, two-hull-form blending is considered by using SR221A and SR221B forms (shown in Figure 8). The operation is performed as follows:

$$\mathbf{P} = (1 - T)\mathbf{P}_{\mathrm{A}} + T\mathbf{P}_{\mathrm{B}} \tag{11}$$

where $\mathbf{P}$, $\mathbf{P}_{\mathrm{A}}$, and $\mathbf{P}_{\mathrm{B}}$ are control points for new hull form, hull A, and hull B, respectively; and T is blending parameter. This approach can directly be implemented into ongoing design work. As is demonstrated later, of practical interest is to find the best compromise between the two hulls with opposite hydrodynamic features in design tradeoff.

2.2.3. Prismatic curve parametric modification. New hull-form is directly correlated with parametric modification of prismatic curve (C_p curve). This idea is an extension of an original scheme used in many shipyards [20]. Figure 11 shows definition of the control parameters, where the area distribution is normalized by that of midship section ($x = 0.5$) for convenience. In the figure, new C_p curve is parametrically given by ΔC_p and ΔL_p, through definition of longitudinal movement of sections, i.e. Δx, which is given by

$$\Delta x = (1 - x)\left\{\frac{\Delta L_p}{1 - L_p} + \frac{x - L_p}{A}\left[\Delta C_p - \Delta L_p \frac{1 - C_p}{1 - L_p}\right]\right\} \tag{12}$$

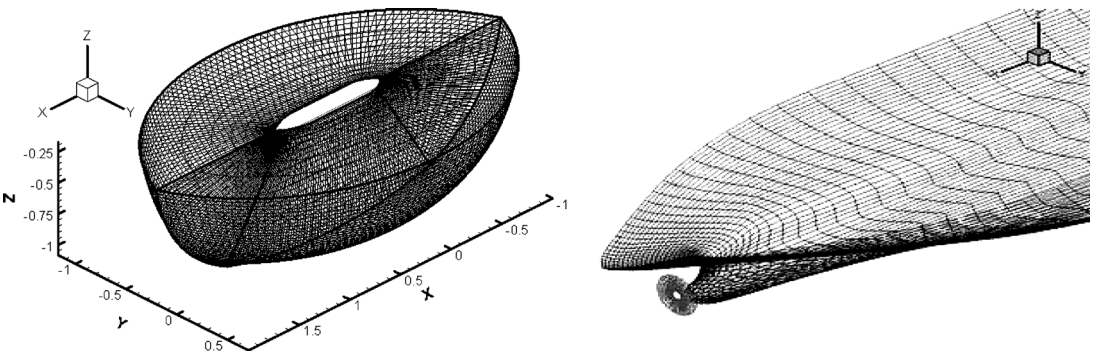

Figure 12. Overview of computational grid. Both port and starboard sides are included in order to account for asymmetric flow due to propeller action.

in association with the following definition of variables:

$$A \equiv C_p(1 - 2\bar{x}) - L_p(1 - C_p) \tag{13}$$

and

$$C_p \cdot \bar{x} \equiv \frac{1}{2}\int_0^1 x^2 \, \mathrm{d}y, \quad C_p \equiv \int_0^1 x \, \mathrm{d}y \quad \text{and} \quad \Delta C_p = \int_0^1 \Delta x \, \mathrm{d}y \tag{14}$$

In the present study, this approach is used in combination with the above-mentioned hull-form blending approach.

2.3. CAD-interfaced automatic grid generator

In the present work, a recently developed CAD-interfaced automatic grid generator is applied. Surface as well as volume grids are automatically generated based on prescribed set-up parameters (which are basically same in series case studies if grid topology is fixed). The volume grid is generated by an elliptic-algebraic method using an exponential scheme, and method of lines. A concern for automatic gridding will be robustness to practical complexities of hull surface. Through preliminarily exercises, the present scheme was shown capable for application to tanker hull-forms, surface combatants, and container ships [32]. In all cases, the grid orthogonality especially near the hull surface is sufficiently maintained. Figure 12 shows several views of the present computational grid, which is categorized as O–O-type topology. The grid includes both port and starboard sides for self-propulsion condition in order to simulate asymmetric flows due to influences of propeller action.

2.4. CFD module (RaNS equation solver—FLOWPACK Version 2004d)

The RaNS code is FLOWPACK version 2004d, which has been developed by the authors for CFD education and research, and design applications for ship hydrodynamics, aerodynamic and fluid engineering [21–23]. In the transition for design applications, multi-block domain decomposition capability is included. At present, FLOWPACK has tight interface with both commercial and author's in-house grid generators. Summary of applications is available in

Reference [22] for full-scale simulation, hull-form optimization, America's Cup down-wind sail system, fully appended sailing boat, parachute, automobiles and others.

The numerical method of FLOWPACK solves the unsteady RaNS and continuity equations with zero or two-equation turbulence model for mean-velocity, pressure and eddy viscosity or turbulence parameters by using a body/free-surface conforming grid. The equations are transformed from Cartesian coordinates in the physical domain to numerically generated, boundary fitted, nonorthogonal, curvilinear coordinates in the computational domain. A partial transformation is used, i.e. coordinates but not velocity components. The equations are solved using a regular grid, finite-analytic spatial and first-order backward difference temporal discretization, PISO-type pressure algorithm, and the method of lines. FLOWPACK is able to consider wavemaking effects by using free-surface tracking approach; however in the present work, the feature is not used.

2.5. *Self-propulsion simulator*

In the present study, we consider a ship propelled by a single propeller located near the stern. It is generally observed that the propeller when developing thrust accelerates the water ahead of it, and this has effect of lowering the pressure around the stern and also increasing the velocity there, both of which effects augment the resistance of the ship. This is called thrust deduction, which will be quantitatively defined below and in nomenclature. In the present study, the propulsive performance is represented by the DHP, which is the power actually used for rotating propeller and one of the most important design parameters in ship design. Another important propulsive factor is the effective wake, which is defined by subtracting propeller-induced velocity from total velocity at the propeller disk. This directly correlates with propeller performance, and is obviously different with the ship wake without propeller-induced effects. The latter is often called the nominal wake in contrast to the effective wake. The wake parameters will be used in the subsequent sections where the results are discussed.

The ship propulsive performance is evaluated by the present self-propulsion scheme [23]. The method consists of three parts, i.e. a RaNS solver, a propeller performance program, and a root finder module to determine propeller rotational speed n_p so that the hull resistance R balances with the propeller thrust T, i.e.

$$T = R \tag{15}$$

In the model scale propulsion test, which is usually carried out in the towing tank during a ship design, difference in skin friction between the model and full-scale ships must be considered as a skin-friction correction, i.e. SFC. This eventually reduces the thrust required to balance with the hull resistance, i.e.

$$R = R_{T(SP)} - \mathrm{SFC} \tag{16}$$

where $R_{T(SP)}$ is the hull resistance for self-propulsion state. In the present study, the SFC is given by using C_{F0M}, C_{F0S}, and ΔC_F, all of which are values for frictional resistances for model and full-scale and for consideration of scale effects and surface roughness, i.e.

$$\mathrm{SFC} = \frac{\rho U^2 S_0}{2}\{(1+k)(C_{F0M} - C_{F0S}) - \Delta C_F\} \tag{17}$$

where subscripts M and S correspond to model and full-scales, respectively. In the present work, these follow values used in SR229 research project described later. Propulsive factors are evaluated when the self-propulsion state is achieved. For example, the thrust deduction factor $1-t$ and DHP are given by

$$1-t=\frac{R_{\mathrm{T(Tow)}}-\mathrm{SFC}}{T}=\frac{R_{\mathrm{T(Tow)}}-\mathrm{SFC}}{R_{\mathrm{T(SP)}}-\mathrm{SFC}} \tag{18}$$

and

$$\mathrm{DHP}=\frac{2\pi n_{\mathrm{p}}Q}{75} \tag{19}$$

where $R_{\mathrm{T(Tow)}}$ is the hull resistance for towing state, and Q is propeller torque. Propeller action effects are included in RaNS equations by the body force approach. The body force distribution is interactively and iteratively determined by propeller performance calculation based on infinitely bladed propeller theory [24], by using free vortex distribution in wake and bound vortex distribution on the propeller disk. The disk is divided into $36\times 5=180$ panels in the present work. Figure 13 shows the overall computational procedure of the present

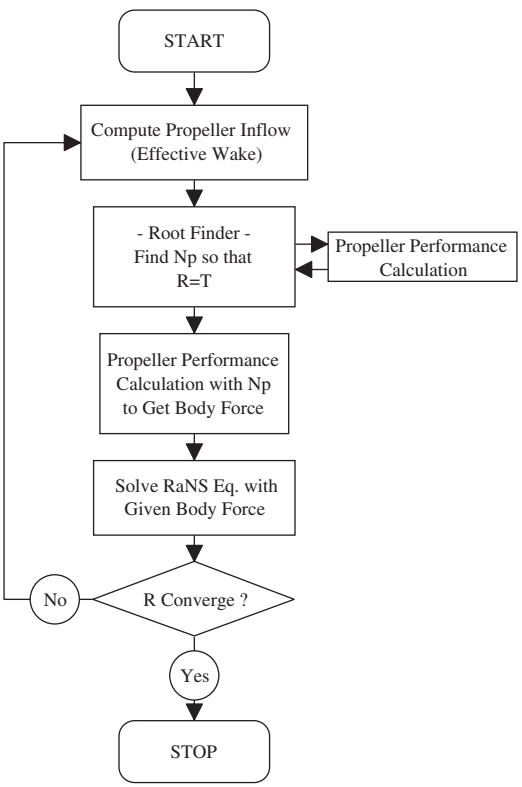

Figure 13. The present self-propulsion scheme. Propeller performance calculation is based on infinitely bladed propeller theory. Root finder determines propeller rotational speed n_{p} so that propeller thrust balances with hull resistance. Thrust deduction and SFC are included for ship-point test.

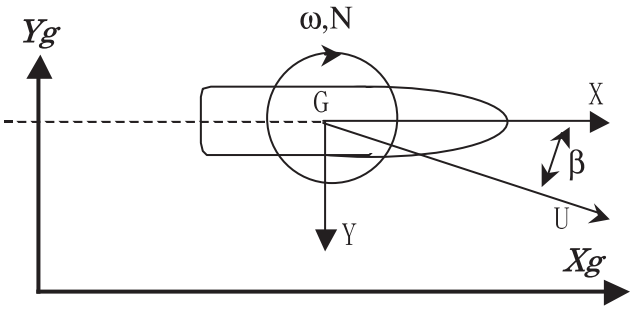

Figure 14. Definition of coordinate system for the present maneuvering simulator.

self-propulsion scheme. Note that flows for self-propulsion condition are computed by using those for towing condition as initial guess. In the present applications, numbers of global sweep iteration in RaNS solver are normally 3000 and 2000 for towing and self-propulsion conditions, respectively. Finally, the DHP directly obtained from the present self-propulsion scheme is used as one of multi-objective functions to be minimized.

2.6. *Ship maneuvering simulator*

The ship maneuverability performance, which is another multi-objective function, is evaluated by using the present ship maneuvering simulator. The scheme was recently developed by the present authors. The method solves the following equation of ship motions for surge, sway, and yaw motions in time-marching manner (see Figure 14 for definition of coordinate system):

$$
\begin{aligned}
F_X &= (m + m_x)(\dot{U}\cos\beta - U\dot{\beta}\sin\beta) + (m + m_y)U\omega\sin\beta \\
F_Y &= -(m + m_x)(\dot{U}\sin\beta + U\dot{\beta}\cos\beta) + (m + m_y)U\omega\cos\beta \\
N &= (I_{ZZ} + i_{zz})\dot{\omega}
\end{aligned} \tag{20}
$$

where m, m_x, m_y, are mass and added masses; I_{ZZ} and i_{zz} are vertical-axial moment and added moment; F_X and F_Y are axial hydrodynamic forces; β and ω are yaw angle and vertical-axial angular velocity; U is ship speed; and dot indicates time derivative. The forces are defined in ship-fixed coordinates X–Y, which are independent from ground-fixed coordinate X_g–Y_g. The hydrodynamic forces are given by the method of Kijima and Nakiri [25] including extensions for tanker hull forms. In the present study, the 10/10 degree-Zigzag test is simulated and the first OSA is used as one of multi-objective functions to be minimized. As shown in Figure 15, the present scheme successfully predicts the trends shown in the measurements for basic hull forms SR221A, SR221B, and SR221C [25]. In the demonstration of optimization, computational values are corrected through the correlation curve shown in the figure, which enables to provide quantitatively more accurate predictions.

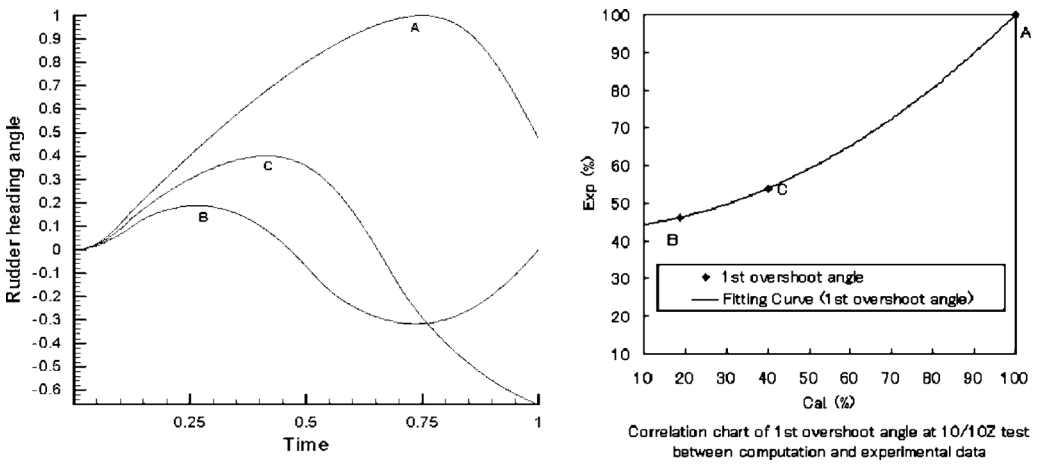

Figure 15. Comparison of the first OSA in 10/10-degree-Zigzag test. Computational results are obtained by using the present ship maneuvering simulator. Trends shown in experiments are correctly reproduced by the present predictions.

3. UNCERTAINTY ASSESSMENT AND ACCURACY IN PROPULSIVE FACTORS AND FLOWS

3.1. Uncertainty assessment

Using the CFD methods, uncertainty assessment must be provided for the solutions and computational grid. CFD uncertainty assessment consists of verification, validation, and documentation. Simulation uncertainty U_S is divided into two components, one from numerics U_{SN} and the other from modelling U_{SM}. The U_{SN} is estimated for both point and integral quantities and is based upon grid and iteration studies which determine grid U_{SG} and iterative U_{SI} uncertainties. A root sum square (RSS) approach is used to combine the components and to calculate U_{SN}, i.e. $U_{SN}^2 = U_{SG}^2 + U_{SI}^2$. CFD validation follows the method of Stern *et al.* [33] and Wilson *et al.* [34], in which a new approach is developed where uncertainties from both the simulation (U_S) and EFD benchmark data (U_D) are considered. The first step is to calculate the comparison error E which is defined as the difference between the data D (benchmark) and the simulation prediction S, i.e. $E = D - S$. The validation uncertainty U_V is defined as the combination of U_D and the portion of the uncertainties in the CFD simulation that are due to numerics U_{SN} and which can be estimated through verification analysis, i.e. $U_V^2 = U_D^2 + U_{SN}^2$. U_V sets the level at which the validation can be achieved. The criterion for validation is that $|E|$ must be less than U_V. Note that for an analytical benchmark, U_D is zero and U_V is equal to U_{SN}. Validation is critical for making improvements and/or comparisons of different models since U_{SN} is buried in U_V.

The above mentioned were applied to evaluate the present CFD method. Table I shows uncertainties and errors for total resistance for KRISO Container Ship (KCS) towing condition test case ($Fn = 0.26$ and $Rn = 1.4 \times 10^7$) [23]. The size of computational grids is about 250 000 and smaller grid is prepared by using refinement ratio $r = \sqrt{2}$, i.e. around 900 000. Order of

Table I. Uncertainties and errors for total resistance.

Uncertainties U_D (%D)	U_G (%D)	U_I (%D)	U_V (%D)
1.0	2.0	0.2	2.2
Errors			
CFD (S)	EFD (D)	E (%D)	
0.00355	0.00356	0.42	

KCS test case for towing condition. $Fn = 0.26$ and $Rn = 1.4 \times 10^7$.

Table II. Comparison of propulsive factors.

	$C_{T(Tow)}$	$1 - w_n$	$C_{T(SP)}$	K_T	K_Q
CFD	0.00355	0.634	0.00393	0.1670	0.0282
EFD	0.00356	0.686	—	0.1700	0.0288
	$1 - t$	$1 - w_T$	η_0	η_R	η
CFD	0.8515	0.789	0.631	1.074	0.732
EFD	0.8530	0.792	0.682	1.011	0.740
	J	n_P (rps)			
CFD	0.718	9.528			
EFD	0.728	9.500			

KCS test case for self-propulsion condition. $Fn = 0.26$ and $Rn = 1.4 \times 10^7$.

accuracy P_G is 1.7, which is given by the previous experience, and the correction factor is given as $C_G = 0.8$. For $C_G = 0.8$ considered as sufficiently less than 1 and lacking confidence, $U_G = 2.0\%$D is estimated. The variation in the total resistance is 0.2%D over the last period of oscillation, i.e. $U_I = 0.2\%$D. Finally, $U_D = 1\%$D and $U_{SN} = 2\%$D yield $U_V = 2.2\%$D. It is shown that the CFD result is validated for the indicated U_V level. In authors' judgment, the agreement between CFD and EFD (experimental fluid dynamics) results is satisfactory for this level of grid size, which is due to a fact that other CFD results recently presented for this test case are generally overestimated and the variation of data was about 5% [32, 35]. Further discussion on propulsive factors will be made in the following section.

3.2. *Accuracy in propulsive factors and flows*

Table II shows comparison of propulsive factors between CFD (i.e. the present self-propulsion simulator) and EFD results for KCS self-propulsion condition test case ($Fn = 0.26$ and $Rn = 1.4 \times 10^7$) [23]. It is shown that generally good agreement is demonstrated. Due to action of propeller, the hull resistance increases about 10%. The increase in hull resistance is mainly due to increase of pressure resistance. Frictional resistance also increases, but the magnitude is insignificant. Influences of propeller action on flows are also correctly reproduced by the present numerical scheme. These are drastic especially in the region right after the propeller. The flow exhibits characteristics of an asymmetric swirling jet and accelerated velocity

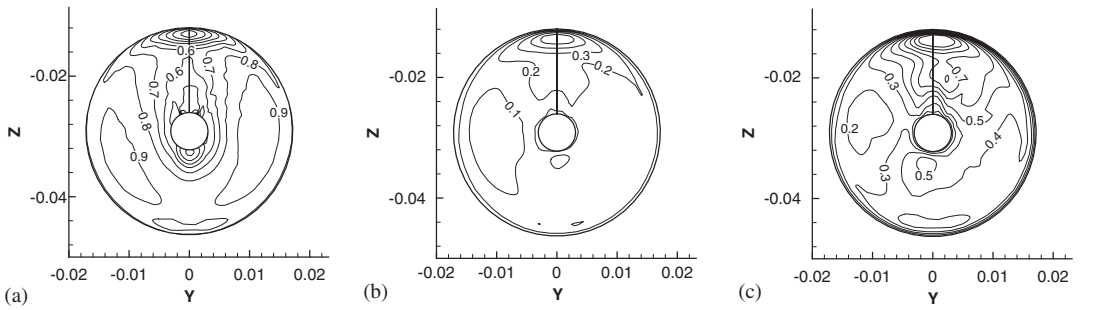

Figure 16. Effective wake, propeller-induced axial velocity, and axial body force contours on propeller disk for with-propeller condition ($Rn = 1.4 \times 10^7$, $Fn = 0.26$): (a) effective wake; (b) propeller induced axial velocity; and (c) axial body force. KCS test case for self-propulsion condition.

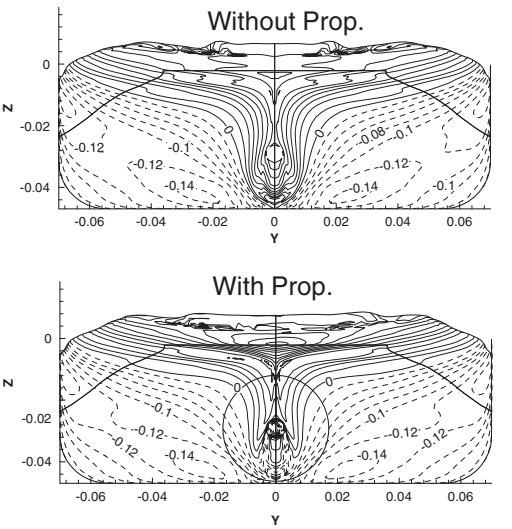

Figure 17. Comparison of surface pressure (C_p) contours between without/with-propeller conditions ($R_n = 1.4 \times 10^7$, $F_n = 0.26$). KCS test cases. Notations 'without/with-propeller conditions' correspond to towing and self-propulsion conditions, respectively.

fields, and importantly, larger acceleration of flow in starboard side than the other side for the given propeller rotational direction (clockwise direction). The present CFD successfully captures such general features of flow [23]. Figure 16 shows the effective wake, propeller-induced axial velocity, and axial body force contours on the propeller disk. Note that effective wake u_e is defined as $u_e = u_t - u_p$, where u_t and u_p are the total- and propeller-induced axial velocity, respectively. Due to the propeller–hull interaction, asymmetric distribution of those values is evident. The axial body force directly correlates with u_p and flows just downstream of the propeller, where the flow is dominated by the propeller-induced effects.

Figure 17 shows comparison of surface pressure contours between towing and self-propulsion cases (without prop. and with prop. in the figure, respectively). The latter case

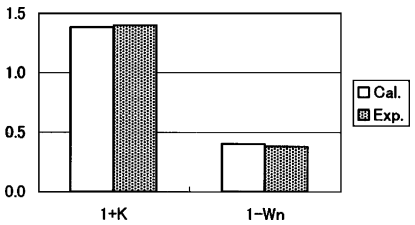

Figure 18. Comparison of $1+k$ and $1-w_n$ between computation and experimental data. SR221B tanker hull form for towing condition.

clearly exhibits expected decrease due to the action of the propeller, which is more evident in the region the boundary layer is thick, i.e. the region near the stern bulb and near the propeller. It is also shown that the influence of the propeller is restricted to the stern region, as is commonly assumed in hull-form design. The trends are also shown in EFD data as backward shift of pressure contours, which agrees well with that predicted by CFD [23].

Accuracy in prediction of resistance and propulsive factors is also evaluated for tanker hull form. The wavemaking effects are not considered. In general, wavemaking effects are neglected in simulation of flow for this type of ship hull, since Froude number of the design speed is generally low, e.g. $Fn=0.15$. This leads to a fact that smaller number of computational grids than the previous case can be used if the main interest is placed on only boundary-layer and wake flows and hydrodynamic forces. Figure 18 shows comparison of form factor $(1+k)$ and nominal wake coefficient $(1-w_n)$ between CFD and EFD results. Although relatively small size grid was used, i.e. 500 000, accuracy in the values is nearly that of experimental data.

3.3. Introduction of CFD–EFD correlation curve for optimization

The above-discussed supports the validity of the present numerical scheme for not only qualitative but also quantitative accuracy if appropriate size of computational grid is used. In reality, CFD-based optimization is time-consuming and size of computational grid is often limited to those which can complete the task within allowable hours. Since a decrease in grid size may yield an increase in simulation uncertainty, it will be difficult to produce results with meaningful improvements if CFD predictions are directly applied.

However, if an optimization aims to search for the best design trade-off and the variation of feasible design modification is relatively limited, the indicated problem can be solved by an alternative approach. Here, we introduced CFD–EFD correlation curves where the correlations between the present CFD and EFD data are examined for basic hull forms SR221A, SR221B and SR221C using a relatively small grid around 200 000. As demonstrated later, the optimal solution is obtained using those basic hull forms. In addition, in order to further reduce computational loads, Baldwin–Lomax model [36] was used in the current study as the algebraic turbulence model. As shown in Figure 19, Results indicate that our computations correctly reproduced the trends in measurements. The same grid size and turbulence model are used through the optimization, where CFD predictions are always corrected using the CFD–EFD correlation curves shown in the figure. The values are considered to be the equivalent of EFD predictions and are therefore used for the evaluation of optimal results.

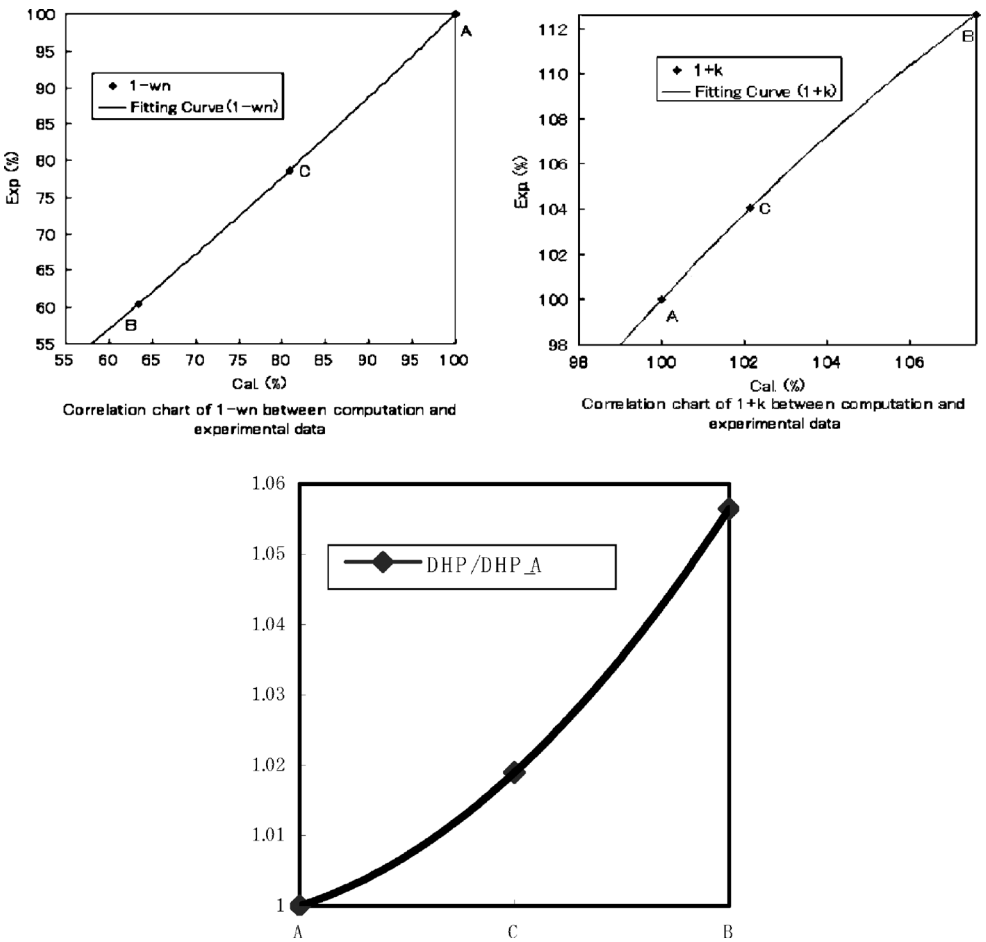

Figure 19. Comparison of propulsive factors between computations and experiments. Trends shown in experiments are correctly reproduced by the present predictions.

4. TANKER STERN FORM OPTIMIZATION PROBLEM

4.1. Hydrodynamic aspects in design optimization

In the determination of tanker stern form, hull-form designers must find the best compromise between the so-called V- and U-shaped stern cross-sections. V-shaped sterns induce weaker stern bilge vortices and lower viscous resistance. In contrast, U-shaped sterns result in generation of stronger vortices and higher viscous resistance; however, the propeller inflow is more uniform with better cavitation characteristics and lower noise. If DHP minimization is performed, flow features to be considered are more comprehensive, i.e. lower hull resistance, better propeller inflow and thrust deduction, all of which are combined effects of propeller–hull interactions. The design tradeoff also occurs when the ship maneuverability is accounted

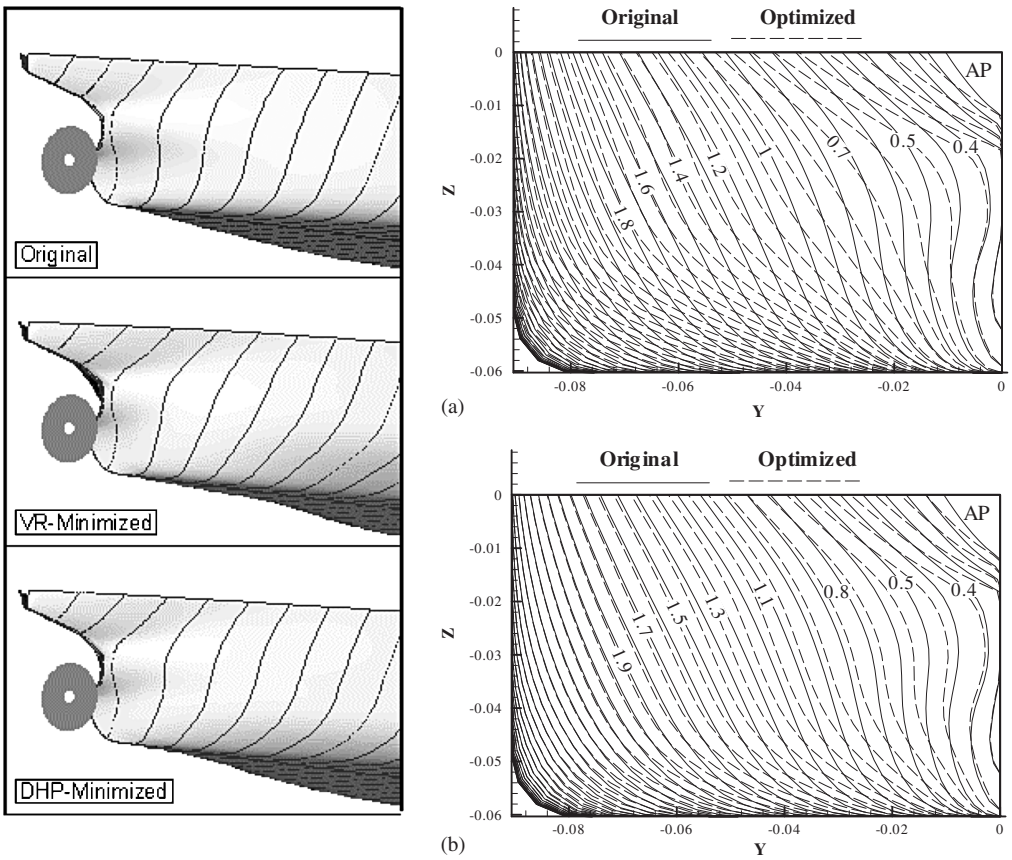

Figure 20. Comparison of geometry between the original and optimized tanker hull forms. Optimized hulls in (a) and (b) are VR-Min. and DHP-Min., respectively.

for, i.e. U-shaped sterns result in better maneuverability performance, e.g. the smaller OSAs in zigzag motions.

In authors' precursory work for tanker stern optimization [4], it was shown that minimum DHP hull form does not coincide with minimum viscous resistance hull form (those are referred to as DHP-Min. and VR-Min., respectively). Earlier version single-objective optimization scheme, CFD and propeller model, and geometry modelling method were used for SR221B stern optimization. Figure 20 shows comparison of geometry between the original and optimal hull forms. Differences in stern frame lines are obvious between the original and optimized hull forms, in which clear differences between DHP-Min. and VR-Min. are also indicated, i.e. frame line modification from U to V types is significant for the latter, in contrast, the trend is somewhat reduced for the former. From U to V frame line modification of VR-Min. results in lower viscous resistance; however, also larger effective wake $(1 - w_t)$ which causes lower propeller efficiency and larger DHP. This implies an important fact that hull-form optimization for minimum viscous resistance does not yield minimum

delivered-horsepower hull form. All of the above-mentioned modification trends agree well with those commonly in use in traditional tanker hull-form design.

4.2. Definition of the present optimization problem

For the complete definition of the design problem to be solved, the following fundamental items must be precisely addressed: (1) selection of an initial design to be optimized and of the extension of the modifiable region; (2) choice of the objective function to be minimized plus number and position of the design variables; and (3) type and quantity of the constraints of the problem. All these items are described in the following.

4.2.1. Initial design. The initial design hull forms are SR221A and SR221B tankers, which were conceived as preliminary designs for VLCC tanker hull forms for extreme V- and U-type sterns, respectively, and selected in Domestic Japan Research Projects ca. 1990. Additionally, SR221C form is examined in the projects as an in-between the two hull forms. All hull forms have the same forepart. All include bulbous bow and stern bulb and are apparently more modern designs than earlier test models SR196 or HSVA tankers. Propulsion is provided through single open-water propeller. There is a large EFD database for SR221 series tankers due to the collaborative study on EFD/CFD and hull-form optimization among universities and shipbuilding industries (SR229, April 1996–March 1999) [37]. The EFD data include measurements on stern flows, propulsive factors, and maneuverability performance. In the present study, bare-hull stern optimization (after midship) is considered including propeller influences, in which the propeller model and the POT characteristics follow those studied in SR229.

4.2.2. Objective function, and functional and geometrical constraints. Complete definition of the problem, objective function and constraints, is given in Table III. For the present demonstration, free-surface effects are not considered. Two objective functions are considered, i.e. (i) the DHP at a speed of $Rn = 3.11 \times 10^6$ at model scale, and (ii) first OSA for 10/10-degree-Zigzag test, all of which are simultaneously minimized. Design Fn is set to 0, since for this hull-form wavemaking effects are negligibly small. Geometrical constraints are imposed on the profile, the design variables, and the displacement and principal dimensions of the ship. In addition, static sinkage and trim conditions are used, which are apparently simplification of the practical optimization problem but justified due to main objective of the present work, i.e. system development and demonstration. More details are given in Table III.

4.2.3. Design variables definition. The design variables are used to explore the design space, and changes in their values correspond to different ship design. As a consequence, those are closely connected with the specific technique adopted to modify the geometry of the ship and the computational mesh, i.e. the geometry manipulation method which is implemented in the overall optimization scheme. Hence, the design variables in the present work are parameters in hull-form blending and C_p curve control, i.e. T in Equation (11), and ΔC_p and ΔL_p in Equation (12). Table III shows constraints for the variables.

Table III. Definition of objective functions and constraints.

Type	Definition	Note
Objective functions		
2 objective functions: propulsive and maneuvering performances	$F_1 = \mathrm{DHP}\ (\boldsymbol{\beta}; Rn, Fn)$	Delivered horsepower at ship-point self-propulsion condition (DHP) and first overshoot angle at 10/10 Z-test (OSA) for $Rn = 3.11 \times 10^6$
	$F_2 = \mathrm{FOA}\ (\boldsymbol{\beta}; Rn, Fn)$	No free-surface effects, i.e. $Fn = 0$
	$\boldsymbol{\beta} \in R^{N_{dv}}$	
Geometrical constraints		
Profile	Profile is fixed	
Variation of design variables	$0 \leqslant T \leqslant 1$	T: Blending parameter
	$-1 \leqslant \mathrm{d}Cp \leqslant 1$	$\mathrm{d}C_p$ and $\mathrm{d}L_p$: C_p curve modification parameters
	$-1 \leqslant \mathrm{d}Lp \leqslant 1$	Bare hull, fixed model. Afterbody (after midship) is optimized
Main dimensions	L_{pp}, D, and B are fixed	
	Forebody is fixed	
Displacement	$\dfrac{\Delta}{\Delta_{\mathrm{Original}(221B)}} \geqslant 0.998$	Minimum displacement is 99.8%Δ of SR221B

5. RESULTS AND DISCUSSION

5.1. Multi-objective optimization environment

The present multi-objective optimization for minimum DHP–OSA was performed on a single CPU Personal Computer (Pentium 4, 2.6 GHz). The system parameters of MOGA are as follows: crossover rate = 1.0, mutation rate = 0.02, population size = 10, and number of maximum generation = 10. For the present multi-objective optimization, Pareto-optimal front obtained in 10 generations is represented as a final solution. Wall-clock time to proceed 10 generations was about 100 h, i.e. about 4 days, which is considered to be within practical turnaround. The time will be considerably shortened by using parallel computing environment [31], but that was not considered in the present work. As already noted, SQP is used for single-objective optimization for minimum DHP, where in this case the convergence criterion was satisfied at eight global optimization cycles. The results are used for verification of multi-objective optimization as described below.

5.2. Optimized hulls

Figure 21 shows Pareto front obtained in 10 generations for multi-objective optimization. In the figure, the individuals which violate design constraints are excluded. Figures 22 and 23 show comparison of body plan, surface pressure and streamlines for the present optimal hull forms. In addition, Tables IV and V show summary of properties and propulsive factors. In the figures and tables, results for original (or basic) hull-forms, i.e. SR221A, SR221B, and SR221C, are also included for comparison. In the tables, all values are expressed in relative% differences to values for SR221A (hereafter, referred to as $\mathrm{S_A}$). In the demonstration of optimization and discussions to follow, computational values are corrected through the correlation curves shown in Figures 15 and 19, which enables to provide quantitatively more accurate

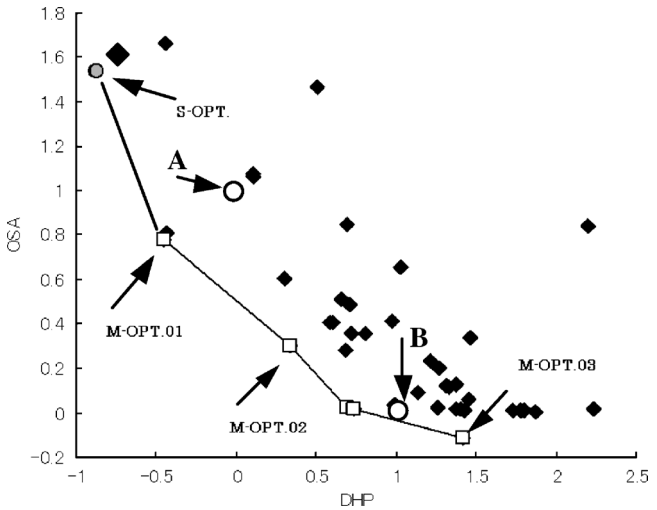

Figure 21. Pareto front obtained in 10 generations for multi-objective optimization.

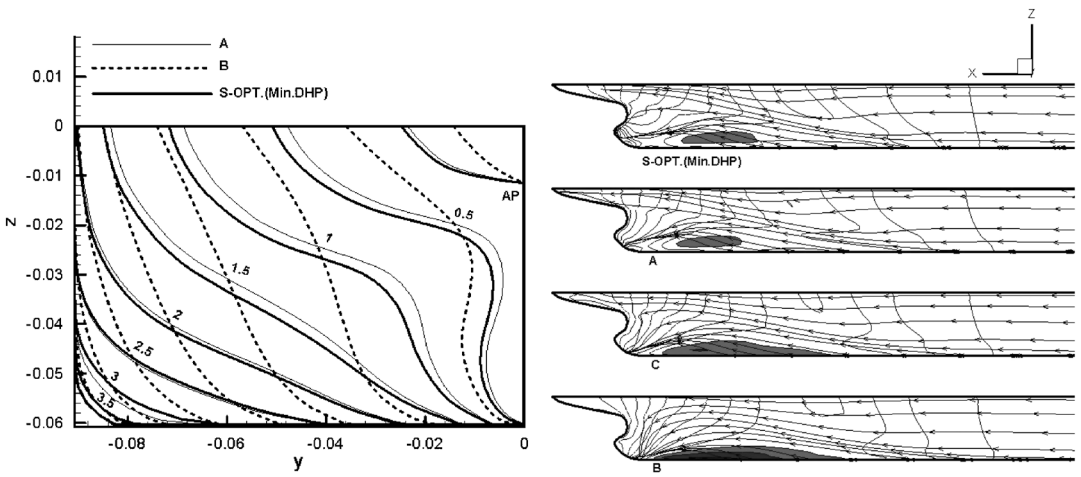

Figure 22. Comparison of bodyplan, surface pressure, and streamlines between the original and single-objective (DHP) minimal hull forms. Shaded area in pressure contours indicates pressure pocket region.

predictions. Notations S-Opt and M-Opt correspond to results for single- and multi-objective optimizations, respectively. It is important to note that all individuals on the Pareto-optimal front in Figure 21 will be candidates for designer's choice. Next task of designers is selection of final candidates, that may be based on designers' own multi-criteria for hydrodynamic performances possibly including other factors in ship-building process. The designer could use a decision-making technique to pick up one final solution among a set of Pareto-optimal

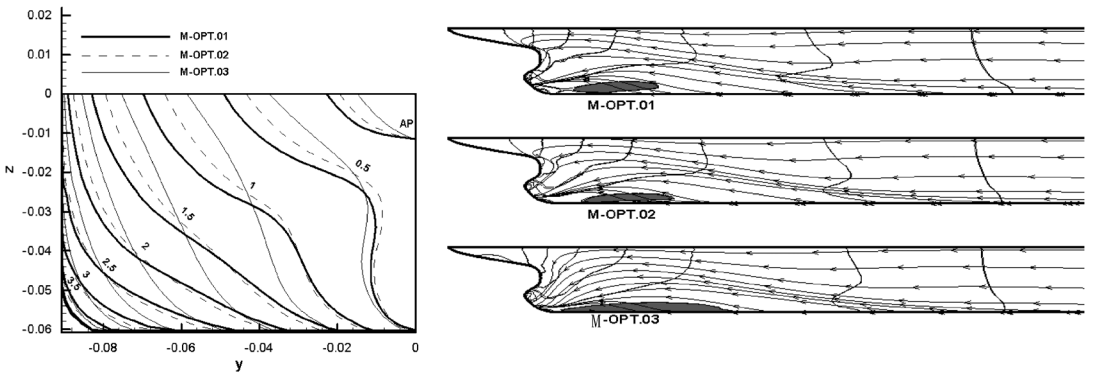

Figure 23. Comparison of bodyplan, surface pressure, and streamlines among optimal hull forms. Shaded area in pressure contours indicates pressure pocket region.

Table IV. Properties and propulsive factors of original and single-objective optimal hulls.*

	Wet. surface (%)	Displacement (%)	$R_{T(Tow)}$ (%)	$1 - w_t$ (%)	DHP (%)
A	0	0	0	0	0
B	−1.21	−0.33	+11.24	−39.52	+5.25
C	−0.86	−0.15	+3.17	−21.29	+2.50
S-Opt.	−0.17	+0.55	−4.50	+7.58	−3.13

*$\%S_A - 100$.

Table V. Properties and propulsive factors of original and multi-objective optimal hulls.*

	Wet. surface (%)	Displacement (%)	$R_{T(Tow)}$ (%)	$1 - w_t$ (%)	$1 - t$ (%)	DHP (%)	OSA (%)
A	0	0	0	0	0	0	0
S-Opt.	−0.17	+0.55	−4.50	+7.58	+1.00	−3.13	+40
M-Opt.01	−0.35	+0.59	+3.25	−14.49	+0.21	−2.25	−17
M-Opt.02	−0.78	−0.14	+4.22	−15.96	+0.86	+1.65	−56
M-Opt.03	−0.94	−0.51	+9.15	−31.77	−0.95	+7.10	−89

*$\%S_A - 100$.

designs. Some examples of the decision-making theory are described in Reference [30]. In the present study, three representative individuals on the Pareto front are selected, namely M-Opt.01–03, and used to discuss the trends in hull forms and flows.

5.3. Numerical results and verification

First, values in Table IV, i.e. those for basic hull-forms, are discussed. Wetted surface areas of basic hull forms SR221B and SR221C are smaller than that of SR221A, i.e. $-1.21\%S_A$ and $-0.86\%S_A$, respectively, and so are displacements, i.e. $-0.33\%S_A$ and $-0.15\%S_A$, respectively. Total resistances for towing condition $R_{T(Tow)}$ are larger, i.e. $+11.24\%S_A$ and $+3.17\%S_A$

for SR221B and SR221C, respectively; but effective wakes $(1 - w_T)$ indicate reverse trends, i.e. $-39.52\%S_A$ and $-21.29\%S_A$, respectively. Resultant DHPs are larger, i.e. $+5.25\%S_A$ and $+2.50\%S_A$, respectively. As mentioned earlier, all of the predicted trends agree well with the measurements.

Next, the above discussions are continued for the optimal hulls (see Table V). Wetted surface areas of S-Opt, M-Opt.01, M-Opt.02, and M-Opt.03 are all smaller than that of SR221A, i.e. $-0.17\%S_A$, $-0.35\%S_A$, $-0.78\%S_A$, and $-0.94\%S_A$, respectively; and displacements are larger for S-Opt and M-Opt.01, i.e. $+0.55\%S_A$ and $+0.59\%S_A$, respectively, and smaller for M-Opt.02, and M-Opt.03, i.e. $-0.14\%S_A$ and $-0.51\%S_A$, respectively. Thrust deductions $(1 - t)$ are larger for S-Opt, M-Opt.01, and M-Opt.02, i.e. $+1.00\%S_A$, $+0.21\%S_A$, and $+0.86\%S_A$, respectively; and smaller for M-Opt.03, i.e. $-0.95\%S_A$. $R_{T(Tow)}$ and $(1 - w_T)$ indicate reverse trends, i.e. $-4.50\%S_A$, $+3.25\%S_A$, $+4.22\%S_A$, and $+9.15\%S_A$ for $R_{T(Tow)}$ of S-Opt, M-Opt.01, M-Opt.02, and M-Opt.03, respectively; and $+7.58\%S_A$, $-14.49\%S_A$, $-15.96\%S_A$, and $-31.77\%S_A$ for $(1 - w_T)$. DHP and OSA also show reverse trends, i.e. $-3.13\%S_A$, $-2.25\%S_A$, $+1.65\%S_A$, and $+7.10\%S_A$ for DHP of S-Opt, M-Opt.01, M-Opt.02, and M-Opt.03, respectively, and $+40\%S_A$, $-17\%S_A$, $-56\%S_A$, and $-89\%S_A$ for OSA. An important fact shown in the present results again supports a conclusion of the author's precursory work [4], i.e. the minimum $R_{T(Tow)}$ hull form does not coincide with minimum DHP hull form, and inclusion of propeller–hull interaction is necessary for meaningful DHP minimization.

It is an expected trend that S-Opt indicates the lowest DHP but the largest OSA. S-Opt has more enhanced V-type stern, and backward movement of volume distribution is seen in. The modification trends yield worsening of effective wake $(1-w_t)$ and thrust deduction $(1-t)$, but lowering of the hull resistance which compensates for the worsening of effective wake and thrust deduction; and finally the combined effects of those result in the lowest DHP among all optimal hulls. The present MOGA finds relatively close neighbours of S-Opt. As the maximum number of generation increases, the closer point to S-Opt will be detected, which is due to the probabilistic nature of the MOGA theory. On the other hand, the trends shown in the sequence of S-Opt, M-Opt.01, M-Opt.02, and M-Opt.03 are found to change in sterns from V to U type. As DHP increases, OSA decreases. More details on hydrodynamic characteristics of those optimal hulls are discussed below.

For all hulls shown in the figures, flows near the stern are closely correlated with surface pressure distributions. The differences are clear for surface pressure distributions and limiting streamlines near the stern. Surface pressure distributions for all hulls indicate pressure pockets near the stern bilge, and those of the U-type stern tend to indicate larger low-pressure region and lower values near the centre of the region. The pressure pockets attract the flows from the side and bottom of the hull, that leads the merging of the flows. The deeper pressure pocket has stronger influences on the flows approaching towards stern, and leads three-dimensional flow separation and generation of stern bilge vortices. As the stern form changes from U to V types, surface pressure indicates smaller region of the three-dimensional flow separation, therefore produces weaker stern bilge vortices and lower viscous resistance. On the other hand, stronger stern bilge vortices yield lower effective wake, which is an advantage regarding propeller performance. Besides, extreme V-type sterns tend to results in worsening of thrust deduction and maneuverability performance. All of the above-mentioned trends in flow features are consistent with trends shown in the present optimal hulls.

As shown in the results, conditions of Pareto optimality are satisfied, so that noninferior points are successfully found by excluding the points **x** dominate point **y**. Besides, optimal hulls on Pareto front are found superior to all initial hull forms. Moreover, the convex Pareto front includes reasonable number of final selections in spite of relatively small population size. These support validity of the present MOGA scheme in association with validity of the present problem definition, where opposite hydrodynamic characteristics in design tradeoff are minimized as multi-objective functions, i.e. DHP and OSA. In summary, results obtained from the present multi-objective optimization appear to be meaningful and very promising, which leads to a conclusion that approach developed and demonstrated in the present work warrants further investigation and extension for more capable CFD-based multi-objective optimization method in practical and productive hull-form designs.

6. CONCLUSIONS

This paper concerns development and demonstration of a CFD-based multi-objective optimization method for ship design. Three main components of the method, i.e. CAD, CFD, and optimizer modules are functionally independent and replaceable. The CAD used in the present study is NAPA system. The CFD method, FLOWPACK version 2004d, is implemented into a self-propulsion simulator, where the RaNS solver is coupled with a propeller-performance program based on infinitely bladed propeller theory in an interactive and iterative manner. In addition, a maneuvering simulation model is developed and applied to predict ship maneuverability performance. The system demonstration is carried out to simultaneously minimize delivered horsepower and the first overshoot angle obtained from the self-propulsion simulator and maneuvering simulation method, respectively. Two nonlinear optimization algorithms are used in the present study, i.e. the successive quadratic programming and the MOGA, while the former is mainly used to verify the results from the latter. In combination with CAD model, a practical hull-form modification method is proposed, i.e. that is based on one-parameter hull-form blending and two-parameter C_p-curve control.

As mentioned earlier, the present work was motivated to overcome limitations appear in most of recent studies related to CFD-based hull-form optimization. The shortcomings are attributed to limitations of a simple geometry modelling and capability of optimization scheme which basically follows single-objective optimization theory. For development of more advanced CFD-based optimization method for practical hull-form design, there were inevitable challenges for introduction of CAD-based geometry modelling scheme and optimization theory for multi-objective optimization problem, in which improvement of a specific aspect of the global design usually causes the worsening for some others. As shown in the present results, the present CAD-based geometry modelling successfully avoids unrealistic hull-form modification and the method can directly be implemented into ongoing design process. Moreover, results obtained from the present multi-objective optimization appear to be meaningful and very promising. All lead to a conclusion that approach developed and demonstrated in the present work is very promising and worthy to further investigate and extend for more capable CFD-based multi-objective optimization method in practical and productive hull-form designs. Extension of the problem and future research direction will involve application to high-speed ship in association with development and adoption of more advanced-level global optimization (GO) algorithms and CFD methods.

NOMENCLATURE

x, y, z	non-dimensional Cartesian coordinates, normalized by ship length L_{pp}
u, v, w	velocity components, normalized by ship speed U_0
U_0	ship speed
ρ	density of water
$Fn = U_0/\sqrt{gL_{pp}}$	Froude number
$Rn = U_0 L_{pp}/v$	Reynolds number
g	gravitational acceleration
v	kinematic viscosity
S_0	wetted surface area at rest
$C_T = R_T/\frac{1}{2}\rho U_0^2 S_0$	total resistance coefficient, where R_T is total resistance
$C_F = R_F/\frac{1}{2}\rho U_0^2 S_0$	frictional resistance coefficient, where R_F is frictional resistance
$C_P = R_P/\frac{1}{2}\rho U_0^2 S_0$	pressure resistance coefficient, where R_P is pressure resistance
$I + k = C_T/C_{F0}$	form factor
C_{F0}	ITTC 1957 frictional coefficient line, $C_{F0}=0.75/(\log_{10} Re - 2)^2$
ΔC_F	roughness allowance
D	diameter of propeller
d_h	diameter of a propeller hub, $d_h = D \times$ (hub ratio)
$J = v_a/n_P D$	advance ratio
$K_T = T/\rho n_P^2 D^4$	thrust coefficient
$K_Q = Q/\rho n_P^2 D^5$	torque coefficient
$K_{Q(O)}$	torque coefficient in open water (uniform flow)
n_P	propeller rate of revolution (rps)
Q	propeller torque
$R_{T(Tow)}$	total resistance in towed condition
$R_{T(SP)}$	total resistance in self-propelled condition
SFC	skin friction correction
T	propeller thrust
t	thrust deduction factor, e.g. $t = (T - (R_{T(Tow)} - \mathrm{SFC}))/T$
$v_a = Jn_P D$	propeller advance speed
w_n	nominal wake, $w_n = \int_0^{2\pi}\int_{d_h/2}^{D/2} ur\,\mathrm{d}r\,\mathrm{d}\theta/(\pi/4)(D^2 - d_h^2)$, where the origin is the centre of propeller
$w_T = (U_0 - v_a)/U_0$	Taylor wake fraction
$\eta = (1-t)/(1-w_T)\eta_0\eta_R$	propulsive efficiency
$\eta_0 = JK_T/2\pi K_{Q(O)}$	propeller open-water efficiency
$\eta_R = K_{Q(O)}/K_Q$	relative rotative efficiency

ACKNOWLEDGEMENTS

This work has been partially supported by the U.S. Office of Naval Research under the grants No. N000140210256 (2002–2005) and No. N000140510616 (2005–2008) through Dr P. Purtell and Dr H. Narita. The authors would like to express their appreciation to Mr I. Kuutti and Mr N. Mizutani at NAPA Oy for their valuable discussions and suggestions.

REFERENCES

1. Tahara Y, Sugimoto S, Murayama S, Katsui T, Himeno Y. *Development of CAD/CFD/Optimizer-Integrated Hull-Form Design System*, vol. 240, J. Kansai Society of Naval Architects, 2003; 29–36 (also a related manuscript was presented at NAPA User Meeting 2003, Helsinki, Finland, 2003).
2. Tahara Y, Himeno Y, Tsukahara T. An application of computational fluid dynamics to tanker hull form optimization problem. *3rd Osaka Colloquium on Advanced CFD Applications to Ship Flow and Hull Form Design*, Osaka, Japan, 25–27 May 1998; 515–531.
3. Tahara Y, Paterson E, Stern F, Himeno Y. Flow- and wave-field optimization of surface combatants using CFD-based optimization methods. *23rd Symposium on Naval Hydrodynamics*, Val de Ruil, France, 2000.
4. Tahara Y, Ando J, Himeno Y. CFD-based optimization of tanker stern form—minimization of delivered horsepower using self-propulsion simulator. *Practical Design of Ships and Other Floating Structures*, Shanghai, China, 2001, 719–724.
5. Tahara Y, Stern F, Himeno Y. CFD-based optimization of a surface combatant. *Journal of Ship Research* 2004; **48**(4):273–287.
6. Peri D, Campana EF, Di Mascio A. Development of CFD-based design optimization architecture. *1st MIT Conference on Fluid and Solid Mechanics*. Cambridge, MA, U.S.A., 2001.
7. Peri D, Campana EF. High fidelity models in the multi-disciplinary optimization of a frigate ship. *2nd MIT Conference on Fluid and Solid Mechanics*. Cambridge, MA, U.S.A., 2003.
8. Peri D, Campana EF. Multidisciplinary design optimization of a naval surface combatant. *Journal of Ship Research* 2003; **41**(1):1–12.
9. Peri D, Campana EF. High fidelity models in simulation based design. *8th International Conference on Numerical Ship Hydrodynamics*, Busan, South Korea, 2003.
10. Peri D, Campana EF. High-fidelity models and multiobjective global optimization algorithms in simulation based design. *Journal of Ship Research* 2005; **49**(3):159–175.
11. Campana EF, Peri D, Tahara Y, Stern F. Comparison and validation of CFD based local optimization methods for surface combatant bow. *25th Symposium on Naval Hydrodynamics*, vol. 5, St. John's, NL, Canada, 2004; 31–46.
12. Tahara Y, Peri D, Campana EF, Stern F. CFD-based multiobjective optimization of a surface combatant. *5th Osaka Colloquium on Advanced Research on Ship Viscous Flow and Hull Form Design by EFD and CFD Approaches*, Osaka, Japan, 14–15 March 2005.
13. Hino T, Kodama Y, Hirata N. Hydrodynamic shape optimization of ship hull forms using CFD. 3*rd Osaka Colloquium on Advanced CFD Applications to Ship Flow and Hull Form Design*, Osaka Prefecture University, Japan, 1998.
14. Minami Y, Hinatsu M. Multi objective optimization of ship hull form design by response surface methodology. *24th Symposium on Naval Hydrodynamics*, Fukuoka, Japan, 2002.
15. Newman III JC, Pankajakshan R, Whitfield DL, Taylor LK. Computational design optimization using RANS. *24th Symposium on Naval Hydrodynamics*, Fukuoka, Japan, 2002.
16. Duvigneau R, Visonneau M, Deng GB. On the role played by turbulence closures in hull shape optimization at model and full scale. *Journal of Marine Science and Technology* 2003; **8**(1):11–25.
17. Hoekstra M, Raven HC. A practical approach to constrained hydrodynamic optimization of ships. *NAV2003 Conference*, Palermo, Italy, June 2003.
18. Brizzolara S. Parametric optimization of SWAT-hull forms by a viscous-inviscid free surface method driven by a different evolution algorithm. *25th Symposium on Naval Hydrodynamics*, vol. 5, St. John's, NL, Canada, 2004; 47–64.
19. Kuutti I. Impacts of product modeling on ship design and production planning. *9th International Conference on Computer Applications in Shipbuilding* (*ICCAS*), Yokohama, Japan, 1997 (also, further information is available at www.napa.fi or NAPA, NAPA Oy Ltd., FIN-00151, Helsinki, Finland).
20. Lackenby H. On the systematic geometrical variation of ship forms. *Trans INA 92*, London, 1950; 289–316.
21. Tahara Y, Hayashi G. *Flow Analyses Around Downwind-sail System of an IACC Sailing Boat by a Multi-block NS/RaNS Method*, vol. 194, J. Society of Naval Architects of Japan, 2003; 1–12.
22. Tahara Y, Katsui T, Himeno Y. Development of simulation based design for ship hydrodynamics and fluid engineering. *4th Conference for New Ship & Marine Technology*, Shanghai, 2004; 1–13.
23. Tahara Y, Wilson R, Carrica P. Comparison of free-surface capturing and tracking approaches in application to modern container ship and prognosis for extension to self-propulsion simulator. *CFD Workshop*, *Tokyo*, *2005*, Tokyo, Japan, 9–11 March 2005.
24. Nakatake K. A practical method to calculate propulsive performance of ships. *Memoirs of the Faculty of Engineering* 1981; **41**(1):87–122.
25. Kijima K, Nakiri Y. *Approximate Expression for Hydrodynamic Derivatives of Ship Manoeuvring Motion Taking into Account of the Effect of Stern Shape*, vol. 98, J. the West Japan Society of Naval Architects, Japan, 1999; 67–77 [Japanese].

26. Campana EF, Peri D, Pinto A, Stern F, Tahara Y. A comparison of global optimization methods with application to ship design. *5th Osaka Colloquium on Advanced Research on Ship Viscous Flow and Hull Form Design by EFD and CFD Approaches*, Osaka, Japan, 14–15 March 2005.
27. Nocedal J, Wright S. *Numerical Optimization*, Springer Series in Operation Research, Springer: Berlin, 1999.
28. Holland J. *Adaptation in Natural and Artificial Systems*. University of Michigan Press, Ann Arbor, Michigan, 1999.
29. Davis L. *Handbook of Genetic Algorithms*. Van Nostrand Reinhold/A Division of Wadsworth, Inc.: New York, 1990.
30. Deb K. *Multi-Objective Optimization Using Evolutionary Algorithms*. Wiley: New York.
31. Tahara Y, Katsui T, Kawasaki M, Kodama K, Himeno Y. Development of large-scale high-performance CFD coding method for PC-cluster parallel computing environment—1st Report: Setup and Initial Evaluation of Coding Environment with MPI Protocol, vol. 241, J. Kansai Society of Naval Architects, 2004; 47–58.
32. *Proceedings of the CFD Workshop*, *Tokyo*, *2005*, Tokyo, Japan, 9–11 March 2005.
33. Stern F, Wilson RV, Coleman HW, Paterson EG. Comprehensive approach to verification and validation of CFD simulations—Part 1: methodology and procedures. *Journal of Fluids Engineering* 2001; **123**:793–802.
34. Wilson RV, Stern F, Coleman HW, Paterson EG. Comprehensive approach to verification and validation of CFD Simulations—Part 2: application for RANS simulation of a cargo/container ship. *Journal of Fluids Engineering* 2001; **123**:803–810.
35. Larsson L, Stern F, Bertram V. Summary conclusions and recommendations of the Gothenburg 2000 workshop. *Gothenburg 2000*: *A Workshop on Numerical Ship Hydrodynamics*, Chalmers University of Technology, September, Gothenburg, Sweden, 2000.
36. Baldwin BS, Lomax H. Thin layer approximation and algebraic model for separated turbulent flows. *AIAA Paper 78-257*, 1978; 1–8.
37. *SR229 Final Report*. Shipbuilding Research Association of Japan, 1999 [Japanese, unpublished].

